Monitoring sea ice with seismic noise

Ludovic Moreau, Agathe Serripierri, Pierre Boué, Jérôme Weiss

MONITORING SEA ICE WITH SEISMIC NOISE

Ludovic Moreau[1] **Agathe Serripierri**[1] **Pierre Boué**[1] **Jérôme Weiss**[1]

[1] Institut des Sciences de la Terre, Université Grenoble Alpes, UMR CNRS 5275, Grenoble, France

ludovic.moreau@univ-grenoble-alpes.fr

ABSTRACT

Field data are needed for a better understanding of sea ice decline in the context of climate change. The rapid technological and methodological advances of the last decade have led to a reconsideration of seismic methods in this matter. In particular, passive seismology has filled an important gap by removing the need to use active sources, hence allowing seismic experiments to be conducted without human intervention in the field. We present a seismic experiment where an array of geophones was deployed on sea ice, in the Van Mijen fjord near Sveagruva (Svalbard). Stations recorded continuously the ambient seismic field in sea ice between 1 and 26 March 2019. From the noise correlation function, the Green's function between the stations of the array is recovered and used to extract the dispersion curves of the ice layer. These dispersion curves are then used in the inverse problem to infer and monitor sea ice thickness and mechanical properties.

1. INTRODUCTION

The effects of global climate changes are strongest in the Arctic, which currently undergoes the most intense warming on Earth, e.g. [1]. A spectacular signature of these changes is the accelerated decline of the sea ice cover, at a rate faster than forecasted by climate models, either in terms of ice extent [2] or average thickness [3]. Recent analyses predict a sea ice-free Arctic as early as 2030 [4]. Hence, understanding this sea ice decline in conjunction with global warming is one of the main challenges of modern climatology. In this matter, a finer description of the dynamic and thermodynamic processes involved in sea ice models is needed. However, accurate parameterization of these models require more complete datasets of sea ice properties: salinity, temperature, mechanical properties, and thickness.

The propagation of seismic waves guided in sea ice has been exploited for decades to develop methods for the monitoring of the ice properties [5–9], which are ingredients for climate and sea ice models. These methods exploit the dispersion characteristics of the guided modes that compose the wavefield. With appropriate forward modeling, an inverse problem can be defined to infer the ice thickness and elastic properties, based on a fit between the dispersion of the guided modes in the model and in the data. Such approaches are quite common, not only in geophysics, but also at the ultrasonic scale for nondestructive testing [10] or medical acoustics [11] applications. As far as sea ice applications are concerned, the main challenge with such monitoring methods are the in situ logistics, which require the deployment of seismic antennae with many geophones, as well as the use of active sources. Given the hostile conditions and the difficulty to access polar environments, these are considered to be the main limitations of such methods, despite their potential for accurate sea ice properties estimations

The present paper is a follow up of our work initiated first at the laboratory scale [12], and then at the geophysical scale [9], to infer the thickness and mechanical properties of the ice from the measurement of guided wave modes. In the former, active piezoelectric sources were used for generating ultrasonic guided waves in the ice layer that grows at the surface of a water tank in a cold room. In the latter, guided wave propagation was recovered from the noise correlation function (NCF). In passive seismology, the NCF is calculated by correlating the ambient seismic noise (or ambient seismic field) recorded between stations pairs. It can be shown that the NCF converges towards the impulse response, or Green's function, of the medium [13, 14]. This allows receivers to be turned into virtual active sources, and the dispersion curves of the guided wave modes can be extracted from the seismic noise in a totally passive way. This method was applied to seismic noise recorded in sea ice in the Van Mijen fjord, near Sveagruva in Svalbard (Norway) to recover the ice thickness, Young's modulus and Poisson's ratio. Here we introduce results obtained for the whole duration of the seismic experiment, between 1 and 26 March 2019. We demonstrate that sea ice properties can be monitored with high accuracy and a temporal resolution of a few hours.

2. MATERIAL AND METHODS

2.1 Array deployment

Between 1 and 26 March 2019, an array of 247 FairFieldNodal Zland geophones (flat frequency response down to the cutoff frequency of 10 Hz for 1-component sensors and 5 Hz for 3-components sensors) was deployed on the ice of Van Mijen fjord in Vallunden Lake (Figure 1a). This part of the fjord, located about 2 km south-east of Sveagruva, is surrounded by a moraine. Because of its connection to the fjord by a canal of width $\sim$10 m, it is subject to tidal flows and forcing. It is a quiet area that is

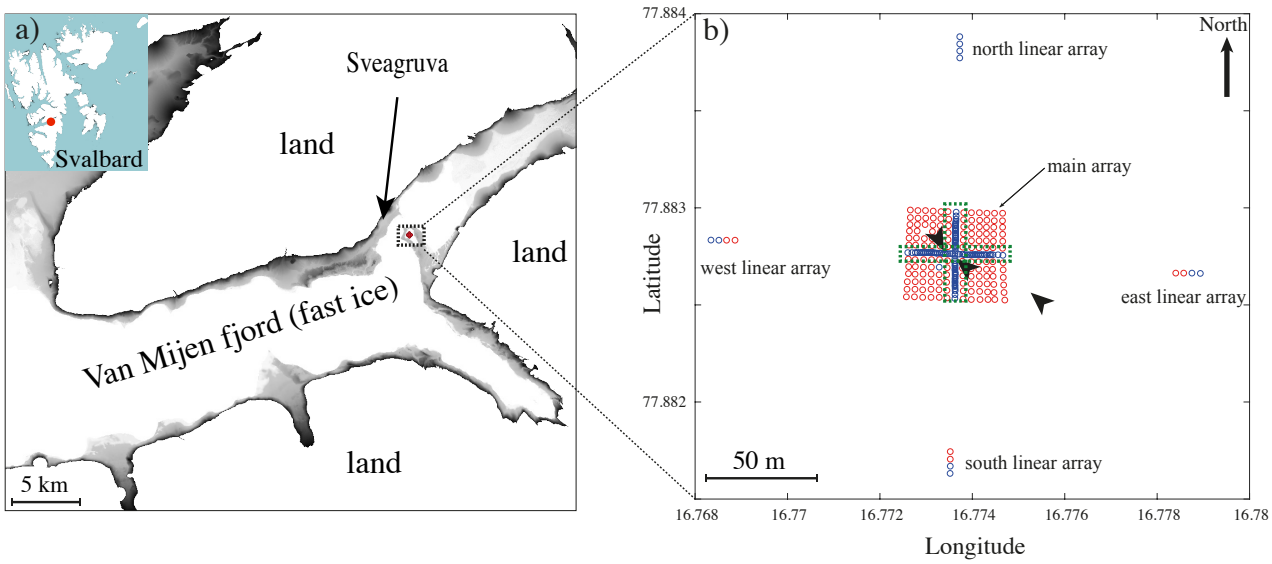

Figure 1. (a) Location of the seismic array in the Van Mijen fjord near Sveagruva (Svalbard), with (b) a zoom around the 247 stations of the array, including the main central array, and the four linear arrays to the north, east, south and west. Red circles are for 1C stations and blue circles for 3C stations. The large arrowheads indicate the positions of ice drillings for thickness measurements. The dashed rectangle indicates the line of stations used as receivers to calculate the dispersion curves from noise correlation function

well suited for scientific experiments on sea ice.

The geophones were divided into five zones, including one large, two-dimensional array, and four smaller linear arrays. The distribution of the sensors is presented in details in Figure 1b with blue and red dots indicating 1C and 3C geophones. The main array is a large squared area with sides of length 48 m (Figure 1b). The other four arrays consist of four stations with an aperture of 12 m. The purpose of the main array is to measure guided waves propagating in all directions. The linear arrays act as distant virtual sources, for the calculation of the noise correlation functions [13, 14]. Figure 2 shows 24h of seismic noise recorded on the vertical channel of the station located at the center of the main array, on 3 March 2019. Note the large number of impulsive signals, which correspond to thousands of icequakes.

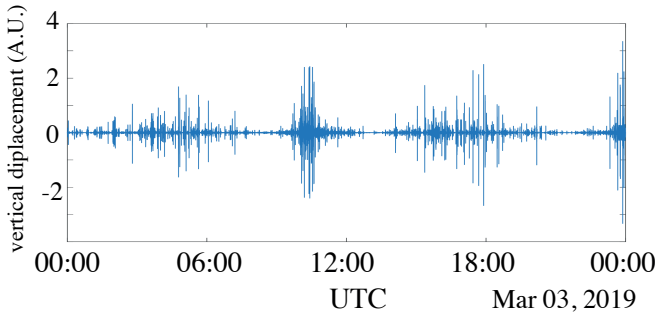

Figure 2. 24 hours of seismic noise recorded on 3 March 2019, on the vertical channel of the station located at the center of the main array represented in Figure 1b.

2.2 Noise correlation function

For the NCF to converge efficiently towards the Green's function of the medium, noise sources have to be stationary and they should have a spatial repartition around the stations that is isotropic. To check the stationarity of the seismic noise, we computed the spectrogram of the recording shown in Figure 2 . The spectrogram indicates that the seismic noise is stationary between 1 and 150 Hz, although there is more energy in the [0-25] Hz frequency band (Figure 3a). To check the isotropy of the noise sources, we compute the slowness vs azimuth beamforming of the seismic wavefield recorded at all stations of the main array (Figure 3b). The beamforming shows that the energy of the seismic wavefield is coming from all azimuthal directions around the array, with a slightly lower amplitude to the south. Note the spatial aliasing limit, which is visible in the [15-17] Hz frequency band. This is because beamforming relies on the spatial coherency of the wavefield. Hence it is sensitive to spatial sampling. As such, it is restricted to frequencies where geophones spacing allows a sampling of the wavelength that satisfies Nyquist's criterion to prevent aliasing. Spatial sampling in the main array is limited by the 1C stations, which are separated by a four-meter spacing. To compute the beamforming, we are therefore restricted to frequencies where the wavelength is at least 8 meters, *i.e.* under 16 Hz for the QS mode.

In order to calculate the NCF, we apply the following pre-processing steps.

- recordings are truncated into 5 minutes-long time segments
- in each segment we apply amplitude normalization

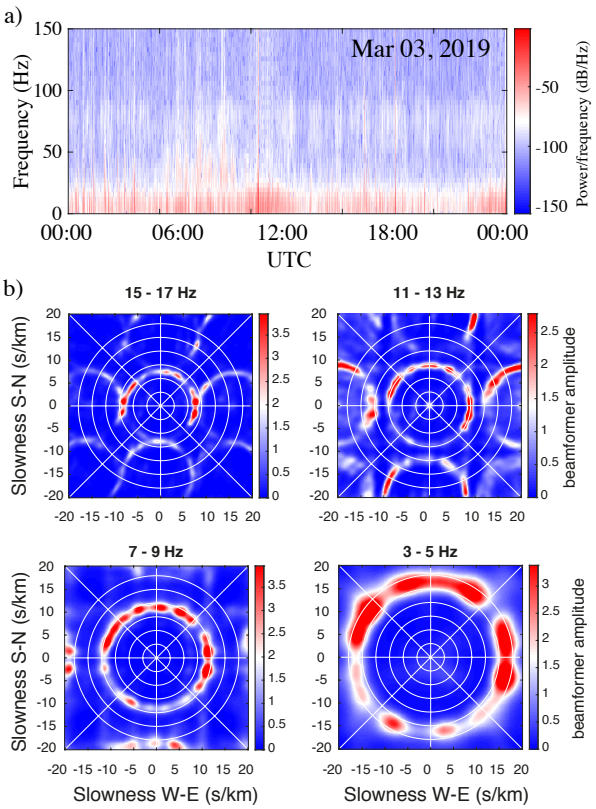

Figure 3. a) Spectrogram of the noise recording shown in Figure 2. b) Beamforming of the same noise recording with the stations of the main array. The distribution of noise sources is isotropic, with a slightly lower amplitude to the south. Note the aliasing limit in the 15-17 Hz frequency band, where the QS mode has a wavelength of about 8 m, causing a duplication of the beamformer that is very close to overlapping itself near the slowness of 8 s/km.

with a sliding window of length 10 s. The choice of 10 s corresponds to the typical length of a waveform after the triggering of an icequake. This allows the NCF to not be dominated by the impulsive signals such as those that can be seen in Figure 2.

- spectral whitening is applied to the resulting signals in order to mitigate the dominance of the low frequency sources
- the resulting segments are finally stacked together

We observe convergence of the NCF for a number of stacks corresponding to about 8 hours of noise recording. An example is given in Figure 4, which shows the causal part of NCF between the station at the center of the main array and the east-most station of the east linear array (see Figure 1). This NCF was calculated with 8 hours of continuous noise on the vertical channel, from 0:00 to 8:00 AM on 1 March 2019. For comparison, the figure also shows the waveform measured at the center of the array when an impulsive source is used at the position of the east-most station. The agreement between the waveform in the NCF and that from the impulsive source is excellent, which confirms the convergence of the NCF.

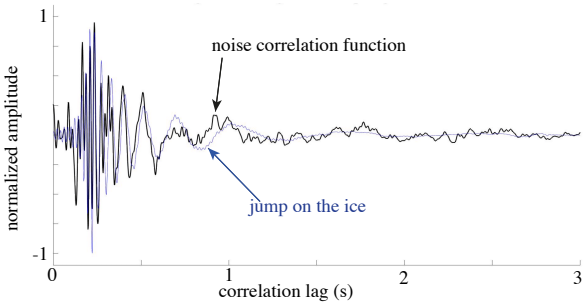

Figure 4. Comparaison between the causal part of NCF calculated between the station at the center of the main array and the east-most station of the east linear array in Figure 1b.

2.3 Extracting the dispersion curves from the NCF

Once the NCF is calculated between every station pair of the array, each station becomes a virtual source for the other stations. Next, we consider the stations in the linear arrays as virtual sources for the dense cross of receivers, which are oriented in the west-east and south-north directions (see the green rectangles in Figure 1b). A classical way of computing the dispersion curves of a wavefield is to apply a Fourier transform to the time and space dimensions of the waveforms recorded along a line of geophones, which yields the frequency-wavenumber spectrum. If several sources are available, the spectra can be averaged over the number of sources. However, signals with a low signal-to-noise ratio (SNR) may result in frequency-wavenumber spectra of poor quality. A better way of taking advantage of several sources consists in combining them, following the processing described in [15]. The reader is referred to [15] and [12] for more details regarding its implementation and application to the present problem. Only the main steps of this processing are outlined here.

1. The matrix of transmit-receive signals has three-dimensions: sources, receivers, and time. The first step is the application of the Fourier transform to the temporal dimension of this matrix.

2. At each frequency, the resulting Fourier-domain matrix is sliced into 2D transmit-receive matrices. These matrices are then decomposed into singular values, with the underlying idea that the different levels of modal energy are distributed onto a set of orthogonal singular vectors. This allows a heuristic separation of the noise and signal subspaces, in a classical way for singular value-based filters.

3. The last step consists of defining test vectors that are representative of the wave propagation problem in the receivers basis, for example plane waves with a given wavenumber. The projection of test vectors onto the singular vectors of the receivers basis

leads to a scalar product that is maximized when the wavenumber in the test vector matches that of the waves in the measured wavefield.

This processing significantly enhances the identification of the dispersion branches in the frequency-wavenumber space, for two reasons: i) the separation of the noise and signal subspaces and ii) the projection of test vectors is not weighted by singular values. Yet the energy information is only contained in singular values, not in singular vectors, which all have a norm equal to unity. Hence, in theory all modes stand out with the same spectrum intensity, despite their different relative energy in the wavefield.

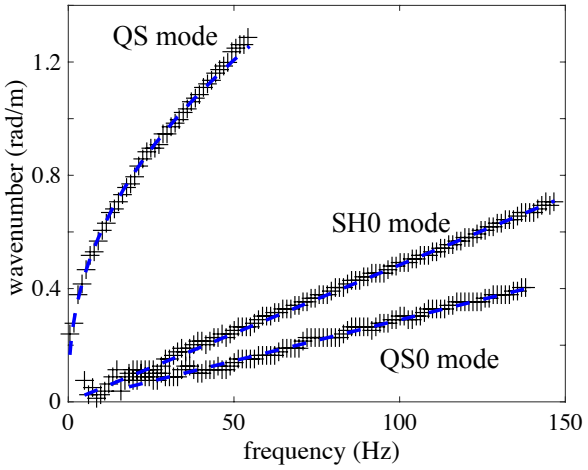

Figure 5. Dispersion curves of the QS, Q_{S0} and SH_0 guided modes obtained from the NCF calculated on 3 March 2019 (+), and from the model ($--$) with the inferred ice properties $h = 0.58$ m, $E = 3.71$ GPa, $\nu = 0.29$ and $\rho = 867$ kg/m^3.

At frequency-thickness values under 50 Hz·m, the three propagating modes, QS, Q_{S0} and SH_0, have a polarization that is mainly in the vertical, longitudinal and shear horizontal directions. Hence the above procedure is applied to the three displacement components to enhance wavenumber extraction. Figure 5 shows the frequency-wavenumber extracted from the NCF on 3 March 2019 between receivers of the west-east direction, and the virtual sources of the east linear array. The three modes appear very clearly in the frequency-wavenumber space.

2.4 Inversion of the dispersion curves

In a layer of ice floating on water, the elastic wavefield contains at least four fundamental guided modes: the quasi-Scholte (QS), quasi-S_0 (QS_0), quasi-A_0 (QA_0) and $SH0$. When the product of the frequency by the thickness of the ice remains under 50 Hz·m, the QA_0 mode is not propagative and the wavefield can be approximated with the combination of the flexural wave, the axial wave, and the shear-horizontal wave [8]. These are essentially the asymptotic behavior of the guided modes, when the displacement field across the ice thickness is considered linear for the QS mode and constant for the QS_0 mode [9].

For a homogeneous waveguide, modal dispersion depends only on the product between the frequency and the thickness of the waveguide. In particular, for sea ice, the only dispersive mode under 50 Hz·m is the QS mode. The following inversion strategy relies on the analysis of the dispersion curves of the guided wave modes propagating in the ice. More specifically, we minimize the least-square misfit between the dispersion curves of the modes measured in sea ice, and those calculated using the asymptotic model by [8]. This is described thereafter.

For an ice layer of thickness h, with Young's modulus, E, Poisson's ratio, ν, and density, ρ, resting on an infinite water column with density ρ_w and speed of sound c, the wavenumber of the quasi-Scholte (QS), quasi-S_0 (QS_0) and $SH0$ modes are given by solving

$$k_{Q_{S_0}} = \omega\sqrt{\frac{\rho(1-\nu^2)}{E}}, \tag{1}$$

$$k_{SH_0} = \omega\sqrt{\frac{2\rho(1+\nu)}{E}}, \tag{2}$$

$$(k_{QS})^4 - \frac{h\rho\omega^2}{D} - \frac{\rho_w}{D}\left(\frac{\omega^2}{\sqrt{\left(\frac{k_{QS}}{\omega}\nu\right)^2 - \left(\frac{\omega}{c_w}\right)^2}} - g\right) = 0, \tag{3}$$

where $D = \frac{Eh^3}{12(1-\nu^2)}$ is the ice-bending rigidity. Next, we set the following values for the water $c_w = 1410$ m/s and $\rho_w = 1010$ kg/m^3. These are standard values for cold water.

Given a set of ice parameters in the model, $\mathbf{X} = [h, E, \nu, rho]$, the above equations are solved for every frequency in the spectrum from the NCF, and a cost function is defined between the dispersion curves in the model, $\mathbf{m}$, and those from the data, $\mathbf{d}$, such that:

$$f(\mathbf{d}, \mathbf{X}) = \frac{1}{3}\sum_{n=QS,Q_{S0},SH_0} ||\mathbf{d}_n - \mathbf{m}_n(\mathbf{X})||, \tag{4}$$

where $||\cdot||$ refers to the L_2 norm.

In order to estimate the density probability function (PDF) of the parameters, we proceed with Bayesian inference, which provides an ensemble of solutions that fit the data with an acceptable level of likelihood, given the data uncertainty. This ensemble of solutions is represented by the posterior distribution of the model parameters, such that

$$P(\mathbf{X}|\mathbf{d}) = \frac{P(\mathbf{d}|\mathbf{X})\,P(\mathbf{X})}{P(\mathbf{d})}. \tag{5}$$

$P(\mathbf{X}|\mathbf{d})$ is the likelihood function, $P(\mathbf{X})$ is the prior distribution and $P(\mathbf{d})$ is the marginal likelihood function, or the model evidence. The posterior distribution expresses the conditional probability of the parameter values based on evidence from measurements, expressed by the likelihood function, and from prior assumptions, expressed by the prior distribution.

The Markov Chain Monte Carlo (MCMC) algorithm is one of several methods that can be used to evaluate

the Bayesian posterior distribution by realizing a Markov chain in the parameter search space. This random walk satisfies the ergodic theorem, which allows the algorithm to converge toward a stationary state that approximates the probability density function (PDF) of the parameters [16]. A recurrent problem in Bayesian inference is the difficulty to calculate the marginal likelihood, which is essentially a normalization factor. However, because it is the same for all probabilities, its determination is not necessary in practice, since it can be cancelled by comparing ratios of probabilities rather than absolute probabilities. This is one of the motivations for using methods based on stochastic sampling such as MCMC.

For the likelihood function, we use a zero-mean Gaussian function with variance σ^2:

$$P(\mathbf{d}|\mathbf{X}) = \exp\left(-\frac{(f(\mathbf{d},\mathbf{X}))^2}{2\sigma^2}\right), \qquad (6)$$

where σ^2 is the variance associated to the measurement errors. This is a typical likelihood function used in many data fitting problems [17]. Moreover, it is also assumed for the prior distribution that the model parameters have equal probability over a finite range of values:

- 0.15 m$\leq h \leq 1.5$ m for thickness
- 2.5 GPa $\leq h \leq 8.5$ GPa for Young's modulus
- $0.1 \leq \nu \leq 0.5$ for Poisson's ratio
- 700 kg/m^3 $\leq h \leq 1000$ kg/m^3 for density

3. RESULTS AND DISCUSSION

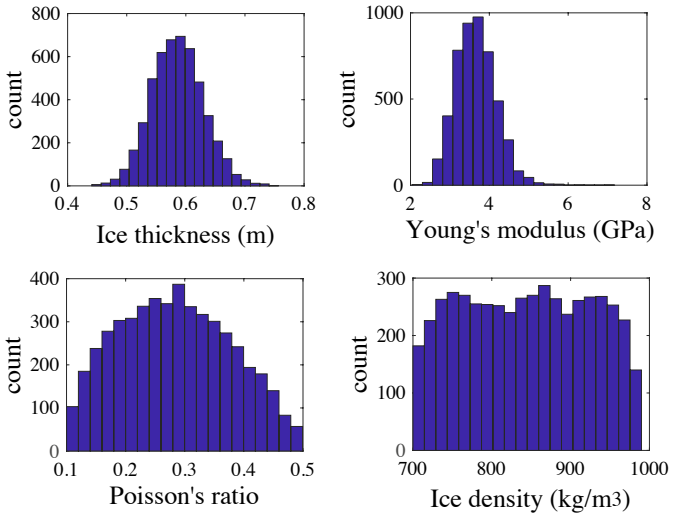

Figure 6. Probability density function of the ice thickness and mechanical properties, estimated from the MCMC algorithm.

Figure 6 shows an example of PDF inferred with the above procedure, for the dispersion curves obtained on 3 March 2019 from the NCF. The ice properties are determined from the Esperance of the PDF. Figure 5 shows the dispersion curves obtained from the Esperance of the PDF in Figure 6, *i.e.* $h = 0.58$ m, $E = 3.71$ GPa, $\nu = 0.29$ and $\rho = 867$ kg/m^3, with an excellent fit between the model and the field data. From the PDF, we note that the ice thickness and Young's modulus are very well-constrained, with a standard deviation of 8 cm and 0.4 GPa, respectively. However, Poisson's ratio is less constrained with a standard deviation of 0.04, and density seems even less well-contained with a standard deviation of 70 kg/m^3.

This inversion procedure was repeated for several days between 1 and 26 March 2019, and for the four directions of propagation: west $\rightarrow$ east, east $\rightarrow$ west, south $\rightarrow$ north, and north $\rightarrow$ south. The inferred ice properties and their standard deviation were averaged over the propagation direction. This is shown in Figure 7.

The ice thickness exhibits a statistically significant increase of about 15 cm. The values found on 1 and 26 March are consistent with values found from ground penetrating radar surveys (52 cm on average on March 1), and from the ice drillings: 62 cm on March 1 and 73 cm on March 26 [9]. This increase of thickness is logical, given the low seasonal temperatures around $-25°$C.

The value of Young's modulus is about half that of fresh-water ice. However, in the Van Mijen fjord, the salinity in March is generally around 6‰ [18]. Brine-liquid volume was shown to vary between 95‰ in 2010 and 30‰ in 2018 [19]. At the place of deployment, the ice contained much brine and was quite porous, with water drawn at the surface from capillarity effect. Young's modulus is known to decrease when porosity and brine content increase [20, 21]. Ice was also very brittle in the top 30 cm. Moreover, the ice in the field had a temperature of about -1°C in the bottom 10 cm. For ice temperatures above -3°C, Young's modulus is significantly reduced [6]. These observations are likely to indicate a gradient of mechanical properties through the thickness. The snow layer covering the ice surface may also have an influence on the apparent Young's modulus [22]. Our onsite radar acquisitions show that the thickness of the snow was comprised between 20 and 35 cm along the dense cross in the main array.

Poisson's ratio has a value of about 0.32 on average and does not vary significantly. This is a standard value for sea ice [21]. The density has a an average value of about 900 kg/m^3, which is also quite standard for sea ice. However, it seems to be the less well-constrained parameter with a standard deviation of about 45 kg/m^3.

4. CONCLUDING REMARKS

This paper presented a proof of concept to use passive seismic data for simultaneously estimating sea ice thickness and mechanical properties. Based on the continuous recording of seismic noise and on appropriate signal processing, we show that broadband propagation of the seismic waves guided in sea ice can be extracted form the NCF. The dispersion curves of three fundamental guided modes are measured in the [1-150] Hz frequency range, and inverted for ice thickness, Young's modulus, Poisson's ratio and density. The inversion procedure is based on the

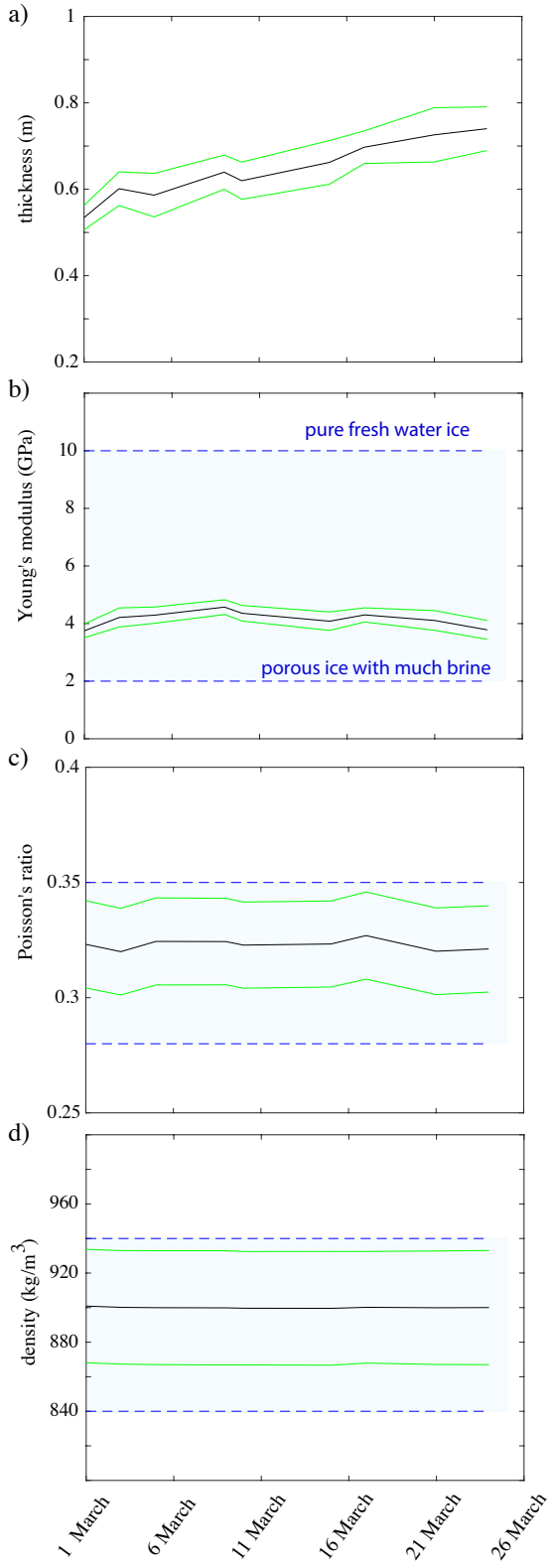

Figure 7. Evolution of the properties of sea in the Van Mijen fjord near Sveagruva (Svalbard) between 1 and 26 March 2019, estimated and averaged over the four directions: east-west, west-east, north-south and south-north. a) thickness, b) Young's modulus, c) Poisson's ratio and d) density. The blue background corresponds to the range of values generally found for sea ice. The error bars represent the standard deviation in the posterior distribution of the parameters, computed with the MCMC algorithm.

MCMC algorithm to infer the probability density function of these parameters. Thickness estimations are in very good agreement with our onsite ground penetrating radar surveys and ice drillings. In comparison with satellite-based estimation methods, this monitoring procedure is shown to estimate sea ice thickness with a much better accuracy. Moreover, we simultaneously invert the mechanical properties of sea ice, and the inferred values are consistent with values reported in the literature, although we noticed that density is not as well-constrained as the other parameters.

By demonstrating that sea ice properties can be monitored based only on passive data (*i.e.* without the need of human intervention in the field, other than for installing the geophones), this study opens locks that had made seismic methods obsolete for sea ice monitoring. This paves the way for new, complementary monitoring strategies where only a very small number of geophones (less than five) is sufficient to estimate the ice properties, for example by analyzing the time-frequency dispersion of the flexural wave measured when icequakes are triggered.

5. REFERENCES

[1] IPCC (2014), Climate Change 2014: Synthesis Report. Contribution of Working Groups I, II and III to the Fifth Assessment Report of the Intergovernmental Panel on Climate Change Rep. 151, *IPCC, Geneva, Switzerland*

[2] Stroeve, J., M. M. Holland, W. Meier, T. Scambos, and M. Serreze (2007), Arctic sea ice decline: Faster than forecast, *Geophys. Res. Lett.*, 34:L09501

[3] Rampal, P., J. Weiss, C. Dubois, and J. M. Campin (2011), IPCC climate models do not capture Arctic sea ice drift acceleration: Consequences in terms of projected sea ice thinning and decline, *J. Geophys. Res-Oceans* **116**(C8), C00D07, doi: 10.1029/2011JC007110

[4] Screen, J.A. and C. Deser (2019), Pacific Ocean variability influences the Time of Emergence of a seasonally ice-free Arctic ocean, *Geophys. Res. Lett.* **46**:2222–2231, doi: 10.1029/2018GL081393

[5] Anderson, D. L. (1958), Preliminary results and review of sea ice elasticity and related studies, *Trans. Eng. Inst. Canada* 2:116-122

[6] Hunkins, K. (1960), Seismic studies of sea ice, *J. Geophys. Res.* 65(10):3459-3472, doi: 10.1029/JZ065i010p03459.

[7] Marsan, D., J. Weiss, E. Larose, and J.-P. Métaxian (2012) Sea-ice thickness measurement based on the dispersion of ice swell, *J. Acoust. Soc. Am.*, 131(1):80–91, doi: 10.1121/1.3662051

[8] Stein, P. J., S. E. Euerle, , and J. C. Parinella (1998), Inversion of pack ice elastic wave data to obtain ice

physical properties, *J. Geophys. Res.* 103(C10):21783-21796

[9] Moreau, L., P. Boué, A. Serripierri, J. Weiss, D. Hollis, I. Pondaven, B. Vial, S. Garambois, E. Larose, A. Helmstetter, L. Stehly, G. Hillers, and O. Gilbert (2020), Sea ice thickness and elastic properties from the analysis of multimodal guided wave propagation measured with a passive seismic array, *J. Geophys. Res-Oceans*, 125(4):e2019JC015709, doi: 10.1029/2019JC015709

[10] Mitra, M. and S. Gopalakrishnan (2016) Guided wave based structural health monitoring: A review *Smart Mater. Struc.*, 14(5):0964–1726, doi: 10.1088/0964-1726/25/5/053001

[11] Bochud, N, Q. Vallet, J.G. Minonzio and P. Laugier (2017), Predicting bone strength with ultrasonic guided waves, *Sci Rep* 7, 43628, doi: 10.1038/srep43628

[12] Moreau, L., C. Lachaud, R. Théry, M. V. Predoi, D. Marsan, J. Weiss and M. Montagnat (2017), Monitoring ice thickness and elastic properties from the measurement of leaky guided waves: A laboratory experiment *J. Acoust. Soc. Am.*, 142(5):2873–2880, doi: 10.1121/1.5009933

[13] Sabra, K.G., P. Gerstoft, P. Roux, W.A. Kuperman and M.C. Fehler (2005), Extracting time-domain Green's function estimates from ambient seismic noise, *Geophys. Res. Lett* 32, 79–84, doi:10.1029/2004GL021862

[14] Shapiro, N. M. and M. Campillo (2004), Emergence of broadband Rayleigh waves from correlations of the ambient seismic noise, *Geophys. Res. Lett.*, 31:L07614. doi:10.1029/2004GL019491

[15] Minonzio, J.-G., M. Talmant and P. Laugier (2010), Guided wave phase velocity measurement using multi-emitter and multi-receiver arrays in the axial transmission configuration, *J. Acoust. Soc. Am.* 127(5) 2913–2919, doi: 10.1121/1.3377085

[16] Andrieu, C. and E. Moulines (2006) On the ergodicity properties of some adaptative MCMC algorithms, *The Annals of Applied Probability* 16(3), 1462–1505, doi: 10.1214/105051606000000286

[17] Tarantola, A. (2005), Inverse Problem Theory and Methods for Model Parameter Estimation, Society for Industrial and Applied Mathematics, Philadelphia, Pennsylvania.

[18] Høyland, K. V. (2009), Ice thickness, growth and salinity in Van Mijenfjorden, Svalbard, Norway, *Polar Research* 28(3):339-352, doi: 10.1111/j.1751-8369.2009.00133.x

[19] Karulin, E. B., A. V. Marchenko, A. N. Sakharov, M. M. Karulina, P. V. Chistyakov , and D. A. Onishchenko (2019), Features of determining the ice flexural strength and the elastic modulus based on floating cantilever beam tests, *Proceedings of the 25th International Conference on Port and Ocean Engineering under Arctic Conditions, Delft, June 2019*

[20] Langleben, M.P., and E. R. Pounder (1963), Elastic parameters of sea ice, in Kingery,, W.D., ed. Ice and snow; properties, processes, and applications: proceedings of a conference held at the Massachusetts Institute of Technology, February 12-16, 1962. Cambridge, Mass., M.I.T. Press, p. 69-78.

[21] Mellor, M. (1986), Mechanical Behavior of Sea Ice, In: Untersteiner N. (eds) The Geophysics of Sea Ice. NATO ASI Series (Series B: Physics). Springer, Boston, MA

[22] Schulson, E. and P. Duval (2009), Creep and Fracture of Ice, *Cambridge: Cambridge University Press*, doi:10.1017/CBO9780511581397